

## Article

# A Self-Activated CNN Approach for Multi-Class Chest-Related COVID-19 Detection

Najam-ur Rehman<sup>1</sup> , Muhammad Sultan Zia<sup>1</sup>, Talha Meraj<sup>2</sup> , Hafiz Tayyab Rauf<sup>3,\*</sup> , Robertas Damaševičius<sup>4</sup> , Ahmed M. El-Sherbeeny<sup>5</sup>  and Mohammed A. El-Meligy<sup>5</sup> 

<sup>1</sup> Department of Computer Science and IT, The University of Lahore Gujrat Campus, Gujrat 50700, Pakistan; 70070155@student.uol.edu.pk (N.-u.R.); sultan.zia@cs.uol.edu.pk (M.S.Z.)

<sup>2</sup> Department of Computer Science, COMSATS University Islamabad—Wah Campus, Wah Cantt 47040, Pakistan; talha\_cui@ciitwah.edu.pk

<sup>3</sup> Department of Computer Science, Faculty of Engineering & Informatics, University of Bradford, Bradford BD7 1DP, UK

<sup>4</sup> Faculty of Applied Mathematics, Silesian University of Technology, 44-100 Gliwice, Poland; robertas.damasevicius@polsl.pl

<sup>5</sup> Industrial Engineering Department, College of Engineering, King Saud University, P.O. Box 800, Riyadh 11421, Saudi Arabia; aelsherbeeny@ksu.edu.sa (A.M.E.-S.); melmeligy@ksu.edu.sa (M.A.E.-M.)

\* Correspondence: h.rauf4@brad.ac.uk



**Citation:** Rehman, N.-u.; Zia, M.S.; Meraj, T.; Rauf, H.T.; Damaševičius, R.; El-Sherbeeny, A.M.; El-Meligy, M.A. A Self Activated CNN approach for Multi-Class Chest-Related COVID-19 Detection. *Appl. Sci.* **2021**, *11*, 9023. <https://doi.org/10.3390/app11199023>

Academic Editors: Anton Civit and Fabio La Foresta

Received: 30 July 2021

Accepted: 21 September 2021

Published: 28 September 2021

**Publisher's Note:** MDPI stays neutral with regard to jurisdictional claims in published maps and institutional affiliations.



**Copyright:** © 2021 by the authors. Licensee MDPI, Basel, Switzerland. This article is an open access article distributed under the terms and conditions of the Creative Commons Attribution (CC BY) license (<https://creativecommons.org/licenses/by/4.0/>).

**Abstract:** Chest diseases can be dangerous and deadly. They include many chest infections such as pneumonia, asthma, edema, and, lately, COVID-19. COVID-19 has many similar symptoms compared to pneumonia, such as breathing hardness and chest burden. However, it is a challenging task to differentiate COVID-19 from other chest diseases. Several related studies proposed a computer-aided COVID-19 detection system for the single-class COVID-19 detection, which may be misleading due to similar symptoms of other chest diseases. This paper proposes a framework for the detection of 15 types of chest diseases, including the COVID-19 disease, via a chest X-ray modality. Two-way classification is performed in proposed Framework. First, a deep learning-based convolutional neural network (CNN) architecture with a soft-max classifier is proposed. Second, transfer learning is applied using fully-connected layer of proposed CNN that extracted deep features. The deep features are fed to the classical Machine Learning (ML) classification methods. However, the proposed framework improves the accuracy for COVID-19 detection and increases the predictability rates for other chest diseases. The experimental results show that the proposed framework, when compared to other state-of-the-art models for diagnosing COVID-19 and other chest diseases, is more robust, and the results are promising.

**Keywords:** chest diseases; COVID-19; transfer learning; deep learning; self-activation; X-ray imaging

## 1. Introduction

Society is developing towards one in which people are more consistently confronted with new and unique diseases. In this industrial era, due to different types of pollution, different diseases, including pulmonological diseases, have arisen. The recent rise of the deadly coronavirus caused a global pandemic. COVID-19 is manifested by pneumonia or chest infections. Different chest diseases are experienced; however, to discover the exact problem or disease in the chest, multiple tests or procedures must be performed. Separate tests and procedures are usually done at one time to identify different chest problems. Many chest diseases cannot be detected with a single test or procedure. X-ray images and convolutional neural networks (CNN) are used to diagnose different diseases. For example, for the coronavirus disease, to detect the virus, an antibody test, a swab test, and other tests are required, but to determine whether the level of chest infection is due to the same virus, we need X-rays in conjunction with other tests for different diseases.

However, using a combination of deep and machine learning, it is much easier to identify different diseases at one time.

A disease is an abnormal situation that impairs the regular functions of any living body and directly affects the condition and structure of all parts of a living organism [1]. Chest diseases are highly aggressive and are one of the most serious health issues faced today. Millions of people face chest diseases globally; tuberculosis, pneumonia, chronic obstructive pulmonary, asthma, and lung cancer diseases are the most common globally [2].

Chronic obstructive pulmonary sickness is a primary source of death and handicap.

Tuberculosis (TB), chronic obstructive pulmonary disease (COPD), pneumonia, asthma, and cellular breakdown in the lungs are considered complex issues and a common cause of death. Pneumonia is a chest abnormality that affects the lungs, where it is a bacterial disease. Early detection of any chest abnormality is a significant factor for effective treatment solutions. Generally, abnormalities can be analyzed from X-ray images by a medical specialist. These diagnoses can be abstract, for example, the presence of diseases can be hazy in chest X-rays or can be mistaken for different chest abnormalities [3]. Asthma is a chest disease that affects approximately 0.3 billion people in the world. It directly affects the human lungs as well, as it is the most common long-term disease of children and adults. Wheezing, breathlessness, chest tightness, and coughing are symptoms of asthma [4]. TB is another chest disease caused by a bacterium known as *Mycobacterium tuberculosis*. TB can directly affect any part of the body, such as the spine, brain, and kidney. For this disease, every year, an average of 0.25 to 0.32 billion cases are reported globally [5]. Asthma, chronic mucus, pneumonia, lingering chest pain, stubborn cough, snorting, coughing up blood, and vocal fold paralysis (VFP) are also common types of chest diseases. Some patients with VFP chest issues are not diagnosed correctly at their first stage. Therefore, these patients may remain untreated for a significant period of time [6].

The coronavirus disease was first reported in China; it has now been declared as a global health emergency by the WHO [7]. It is a respiratory disease and reaches into the respiratory tract and the lungs. Chest CT scan is the most utilized modality for the identification and follow-up of lung abnormalities [8]. Most pediatric chest infections are sufficiently assessed with chest radiography. Chest radiography does not permit the identification of the area and nature of a territory of expanded murkiness, but ultrasonography can contribute toward an analysis [9].

In medical imaging examinations, chest X-rays are the most common and cost-effective exam available. They are used for testing in clinical analysis, but sometimes it is difficult to identify chest diseases due to inexperienced X-ray technician mistakes, not highlighting ROIs, etc. Indeed, some encouraging work utilizing deep learning has been done on whether TB classification or single COVID-19 detection tests are effective.

Many researchers have worked on the identification of chest issues [10–15]. Chest X-ray image filtering is frequently utilized by radiologists to analyze numerous chest-related diseases in their underlying stages [16]. The framework can indeed help radiologists in more effectively identifying diseases found in cleaned X-ray images [17]. Artificial intelligence (AI) techniques guarantee quick and exact identification and forecasts of COVID-19 from standard-of-care chest radiographs and other processed tomography chest images [18]. However, proposed study mainly focuses on multi-class chest disease detection including COVID-19 that is essential need of current era. Due to similar symptoms, any other chest disease can be wrongly diagnose as COVID-19 that may leads to severe health results.

The contribution of this study is as follows:

- The proposed study considers multimodal chest diseases, including COVID-19.
- Self-CNN improved accuracy with a multi-validation method enhances the robustness of the proposed framework.

This paper shows the achievability of detection abnormalities in X-ray images utilizing DL approaches that depend on non-clinical methods. The deep CNNs learn more significant image representations.

The custom CNN design comprises five types of layers: a convolutional layer, a pooling layer, an activation layer, a fully connected layer, and a soft-max activation function that outputs the likelihood for each type of chest disease. Furthermore, transfer learning is applied on proposed DL model that increases accuracy to detect chest diseases using ML classifiers.

The rest of the article is divided into four sections. Section 2 describes previous state-of-the-art work related to chest diseases. Section 3 discusses the proposed system, including the working methodology. Section 4 represents the experiment setup and results. The study is concluded in Section 5.

## 2. Background and Literature Review

The purpose of this study is to provide a more efficient and robust solution to the current problem of chest disease detection. An overview of previously proposed studies indicates solutions proposed by other authors. Many automatic techniques are used for solving different problems. AI systems are becoming the core of many real-time and data science-related solutions, including those for COVID-19 [19,20]. Machine learning (ML) methods can be found in science, technology, health care, manufacturing, education, policing, and marketing [21]. DL is a sub-type of ML that works on deep neural network data representations in a supervised, semi-supervised, or unsupervised way [22,23]. DL techniques are used for the execution of different medical imaging-related tasks [24,25]. In radiology, deep learning can improve the precision of X-ray image segmentation and disease diagnostics. DL methods combined with transfer learning from pre-trained models such as ResNet18, InceptionV3, Xception, MobileNetV3, and DenseNet121 can be used for chest X-ray image segmentation, detection, recognition, and classification tasks [26].

In chest imaging, there has been an effort to create and apply computer-aided detection (CAD) frameworks for the identification of lung lesions on chest radiographs [27,28] and chest tomography [29]. A scan of a patient's lungs using CT/X-ray is used to identify COVID-19, which can cause significant chest abnormalities that require a multimodal chest detection system for chest disease diagnosis.

CNN-based approaches have acquired prominence because of their capacity to learn mid-level and high-level image representations. In [30], the authors show the possibility of recognizing different chest pathologies in chest X-rays using convolutional and DL methods. Different CNNs are introduced for the analysis of chest abnormalities. Back-propagation neural networks are used with the supervised learning backend phenomenon, and competitive neural networks with a backend of unsupervised learning have been built for identifying chest infections.

There are a couple of works focused on multi-class pathological X-ray images, where COVID-19 also needs to be included [31]. Abnormal CT signs such as those of COVID-19 patients at our medical centers need to be analyzed. The acknowledgment of these highlights with medical specialists must be fortified by such signs, which will help them make quick and precise decisions [32]. Remarkably, only 56% of early patients of COVID-19 had a typical CT-X-ray test. However, some time after the beginning of indications, CT discoveries were more frequent, including consolidation, reciprocal and fringe illness, complete lung infections, severe opacities, "insane clearing", and "opposite halo" types. Reciprocal lung association was found. In 28% of early patients, 76% of transitional patients, and 88% of late patients, infectious lungs were diagnosed at different stages from a certain range [33].

The point of examination was to research chest (CT) images of confirmed COVID-19 patients and to assess their relationship with clinical findings. This study considered 80 patients with COVID-19 diagnoses from January to February 2020. The chest CT images and other diagnosed information were reported, and the relation between them was examined [34]. The author presented chest CT discoveries from five patients with COVID-19 infection who had introductory negative, inverted polymerase chain response (RT-PCR) reports. Each of the five patients had regular medical discoveries, including ground-glass

opacity, a blended type, and a mixed combination of chest abnormalities [35]. The role of CT images as an aid to or substitution to RT-PCR in finding COVID-19 and pneumonia has been a subject of debate [36]. There are many diseases of the chest, and we can identify them using machine learning. One way to identify asthma endotypes is to utilize advances in information-driven strategies, with the suspicion that examples of indications or potential biomarkers were surveyed either longitudinally (e.g., in birth co-founders) or cross-sectionally (e.g., in investigations of patients with asthma) [37]. In another paper, the aim was to improve on the medical use and to extend the precision level of the forced oscillation technique (FOT) for identifying asthma. However, the researchers utilized various methods such as k-nearest neighbor (KNN), AdaBoost, random forest (RF), and the feature-based dissimilarity space classifier [38].

The paper in [39] portrayed records of patients with chronic obstructive pulmonary disease (COPD) who were hospitalized for intensive care to meet the expense of such hospitalizations. For highly endangered patient subgroups, other distinguishing factors were possibly connected to a danger of rehospitalization. An AI model was used to consider the variables related to the danger of rehospitalization utilizing choice tree examination. Another direct cost examination was performed from the point of view of public medical insurance.

A precise survey of articles that utilize AI techniques to distinguish clinically significant COPD phenotypes was performed in [40]. Lately, the developing utilization of AI calculations, bunch investigations specifically, has the potential to establish this grouping via joining other explanatory attributes, comorbidities, genomic data, and biomarkers. This combination will permit scientists to more dependably recognize new types of COPD phenotypes, to better describe existing ones, and to improve conclusions and create novel medicines.

The aim of [41] was to find the potential relationship between cellular breakdowns in the lungs and thereby help clinicians and consequently patients to distinguish cellular breakdown in the lungs using these normal tests. Random forest was adopted to assemble a recognizable proof model between routine blood records and cellular breakdown in the lungs that would decide whether they were intensively connected. There are few recent studies have also used the Ai-driven approaches using Regression [42] and Classification methods to detect the COVID-19 and other lungs infections using time-series, pathological, CT, and X-ray data [43–47]. However, some of them are discussed. The time-series data, used in many studies [48–50], are shifted into normalized form using a regression method where later a multi-layer perceptron is used for training purpose [51], it also used in many other studies [52,53]. Similarly, Indian COVID-19 pandemic-based regression is performed on Kaggle data [54], US data are also used in another study [55], as are data from Mexico [56] and Indonesia [57]. Although, some of the studies are given health measures to make effective prevention against COVID-19 [58]. Moreover, the system behavior after government applied policies regarding COVID-19 is analyzed [59]. The evolutionary algorithms also used by various studies to estimate the COVID-19 [60], such as in [60] where optimization algorithms were also used to optimize the proposed methods of COVID-19 identification [61].

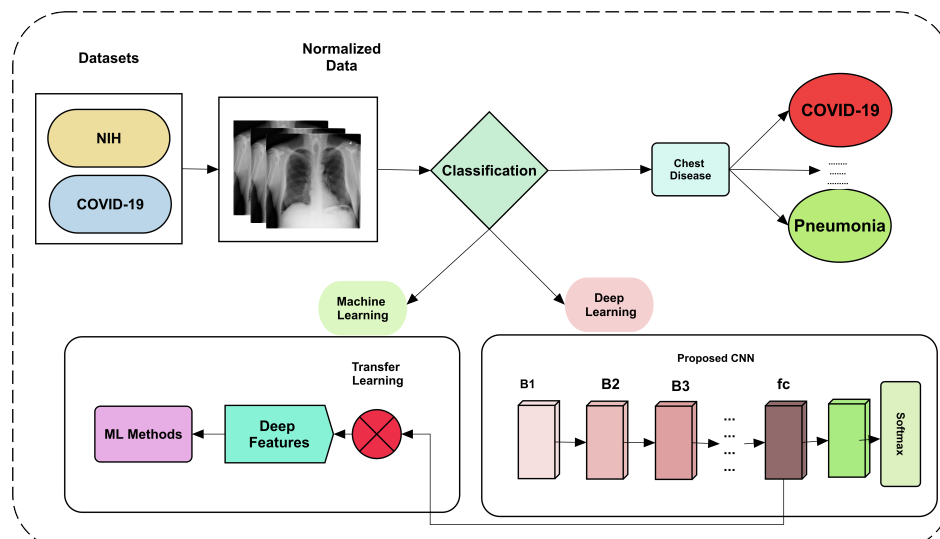
Table 1 shows a summary of previous work.

**Table 1.** Summary of recent studies on the detection of chest-related diseases.

Title of the Paper	Reference	Tools/Classifiers Used	Training Images Used	Dataset(s)	Accuracy
Disease Staging and Prognosis in Smokers Using Deep Learning	[62]	CNN	1000	-	74.95%
Deep Learning for Screening COVID-19	[63]	(DL) (ML)		COVID-19 datasets	90.13%
A Deep Neural Network to distinguish COVID-19	[64]	CNN	108,948	-	87%
Chest CT manifestations of new coronavirus	[31]	GGO	21 patient	-	98%
Chest CT Findings in Coronavirus Disease-19	[65]	Ct scan	125 patient	-	88%
Chest disease radiography in twofold: using convolutional neural networks and transfer learning	[66]	CNN		Chest x-ray dataset	97%
Pneumonia detection on chest x-ray using machine learning paradigm	[67]	ML		Chest x-ray14 dataset	95.8%

### 3. Methodology

In this study, a framework is proposed for the detection of chest diseases, including COVID-19. First, we train our proposed 32-layer CNN and classify the chest diseases using soft-max activations. After that, transfer learning is applied on fully-connected layer of trained CNN. It extracted deep features that were fed to ML classification methods. We then perform 10-fold and 5-fold validation on best performed of the seven machine learning classifiers. The proposed framework in its first stage takes an image as an input and subsequently applies preprocessing to normalize the data. The processing of the proposed framework with primary steps is shown in Figure 1.

**Figure 1.** The proposed framework containing all steps for classification of chest diseases.

### 3.1. Dataset

There are many datasets used for the identification of chest diseases, but we selected these two datasets because our proposed system identifies chest diseases and COVID-19 issues. We selected the NIH and Open COVID-19 X-ray datasets. The datasets of X-ray modality for both chest and COVID-19 diseases have been merged to obtain single-unit data. Due to the size difference, the data were resized in a preprocessing step to normalize it.

### 3.2. NIH Chest X-ray Dataset

In this dataset, the publicly provided improved rendition (with six more infection classifications) of the dataset is utilized in the new work, which has a much higher number of frontal chest X-ray images. It achieved clinically important information for recognition and determination of CAD systems where all information settings of chest X-rays on clinical sites are still troublesome. However, it is certainly feasible when large numbers of images are utilized for any study. This dataset is separate from the clinical PACS information based on the National Institute of Health Clinical Center (NIH) and comprises 60% of all frontal chest X-rays in the emergency clinic where 14 different chest disease data are utilized in proposed study.

### 3.3. COVID-19 Chest X-ray Image Dataset

In the analysis of COVID-19 infection, chest X-rays are a significant part of the analysis of COVID-19 infection, as they contain clarified picture datasets. Multi-class chest disease identification including COVID-19 disease is needed. Therefore, the data from NIH and COVID-19, available at kaggle, were collected and normalized. The number of images for each class is kept equal to avoid overfitting and bias. The normalized images with their selected number and dimension are shown in Table 2.

**Table 2.** NIH chest X-ray and COVID-19 chest X-ray image dataset.

Datasets	Total Images	Size	Classes/	Image Format
NIH Chest X-ray Dataset	2800	1024 × 1024	14/200	PNG
COVID-19 Chest X-ray Image Dataset	200	1024 × 1024	1/200	PNG

In Table 2, the size of these images in the dataset is  $1024 \times 1024$ . The extension is Portable network graphics (PNG). There are 200 images per class.

### 3.4. Data Preprocessing

Preprocessing is a significant step in the data mining process. The expression “trash in, trash out” is especially applicable to information mining and AI projects. Data gathering strategies are regularly approximately controlled, with out-of-range esteems, impossible information mixes, missing qualities, etc. A preliminary processing of information is set up for primary preparation or for additional examination. Data preprocessing is a cycle of setting up raw information and making it appropriate for an AI model. It is the first and pivotal advance in making an AI model robust. Data cleaning and normalization are techniques used to eliminate anomalies and normalize the information. It takes a structure that can be handily used to make a model. Normalization is an information-based design technique that decreases data redundancy and eliminates unwanted qualities such as insertion, deletion, and update anomalies. The described normalization rules separate larger tables into smaller tables and connect those utilizing connections. Mathematically, the normalization equation is represented as given in Equation (1):

$$x_{norm} = \frac{x - x_{min}}{x_{max} - x_{min}} \quad (1)$$

where  $x$  is the input variable as the individual input,  $x_{min}$  and  $x_{max}$  are the minimum and maximum values from that particular feature, and  $x_{norm}$  is the output of the processed input value.

However, the images have pixels that are taken as intensity values. The normalization in these images is somehow different in the context of numeric operations. For this purpose, different interpolation methods have been used in matrix normalization. The data become loss-free when we increase or decrease the input image dimensions. The bilinear interpolation method has been used to preprocess the images. In image processing tasks, the neighborhood pixels are utilized in most cases to obtain focused pixel results. Similarly, in the bilinear method, the  $2 \times 2$  neighborhood operation is utilized to obtain the weighted average. The horizontal and vertical interpolations are performed using corner points of the given input image as points of reference for further operations. Assume the 4 corner points as  $C_{(1,1)}$ ,  $C_{(2,1)}$ ,  $C_{(1,2)}$ , and  $C_{(2,2)}$  as given in Equations (2)–(5).

$$C_{(1,1)} = \frac{(\alpha_2 - \alpha)}{(\alpha_2 - \alpha_1)} \frac{(\beta_2 - \beta)}{(\beta_2 - \beta_1)} Q_1 \quad (2)$$

The vertical corner points  $C_{(1,1)}$  and  $C_{(2,1)}$  are shown in Equation (2) and (3), where  $\alpha$  is the middle point regarding the  $x$ -axis between  $\alpha_1$  and  $\alpha_2$ . The middle point is considered as the  $2 \times 2$  neighborhood, where  $\beta$  is taken as the  $y$ -axis point, and  $\beta_1, \beta_2$  are the corresponding  $2 \times 2$  neighbors of the middle  $y$  point of the considered interpolated point.  $Q_1$  and  $Q_2$  are the quadrants of the four points of the image.

$$C_{(2,1)} = \frac{(\alpha - \alpha_1)}{(\alpha_2 - \alpha_1)} \frac{(\beta_2 - \beta)}{(\beta_2 - \beta_1)} Q_2 \quad (3)$$

Equations (4) and (5) are the corner points of the bottom of a given digital lattice. These points are shown in Figure 2.

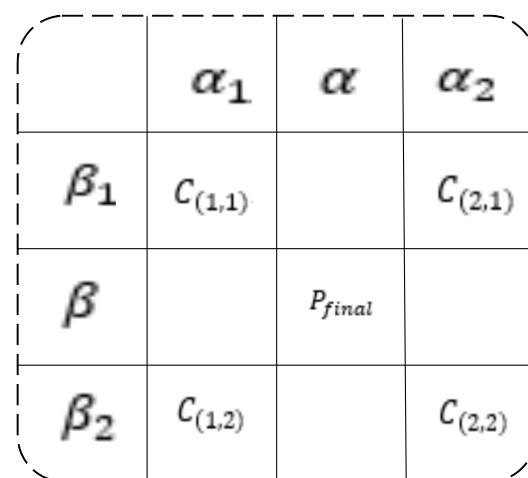


**Figure 2.** Bilinear interpolation method to find the final point ( $P_{final}$ ) for the newly interpolated point.

The four corner points with their corresponding  $2 \times 2$  neighbors for the final point calculations have been shown for a better understanding and interpretation of the given equations of the bilinear interpolation method.

$$C_{(1,2)} = \frac{(\alpha_2 - \alpha)}{(\alpha_2 - \alpha_1)} \frac{(\beta - \beta_1)}{(\beta_2 - \beta_1)} Q_3 \quad (4)$$

$$C_{(2,2)} = \frac{(\alpha - \alpha_1)}{(\alpha_2 - \alpha_1)} \frac{(\beta - \beta_1)}{(\beta_2 - \beta_1)} Q_4 \quad (5)$$

As calculated in Equations (2) and (3), by determining the two corner points  $C_{(1,2)}$  and  $C_{(2,2)}$ , the final point  $P_{final}$  is calculated by the summation of all of them, as given in Equation (6).

$$P_{final} = C_{(1,1)} + C_{(2,1)} + C_{(1,2)} + C_{(2,2)} \quad (6)$$

### 3.5. Classification

The proposed study has used two methods of classification for multi-chest disease detection: (1) the Deep learning and (2) Machine learning methods. In Deep Learning, the proposed study used a proposed architect of CNN where in Machine learning-based Classification, the transfer learning is applied on proposed CNN fully-connected layer that returns the deep features and then fed them as input data to Machine Learning classifiers.

#### 3.5.1. Deep Learning Based Classification

There are many ways of doing classification and other tasks using DL methods such as multi-layer perceptron, autoencoders, etc. but the most commonly used DL method for image based classification is CNN that uses convolve operation in its layers. Similar to this, we propose a CNN architect that is discussed in detail.

#### 3.5.2. Proposed CNN

CNN stands for Convolutional Neural Network, a specific neural network for handling information that has a 2D input shape. CNNs are ordinarily utilized for image detection and classification. In this stage, we train our CNN. The proposed CNN is based on a 32-layer architecture. The size of input images is set  $1024 \times 1024$ . The images are fed to Convolutional Blocks where our convolutional blocks include a sequence of 4 layers (Convolution, batch-normalization, ReLU, and Max-Pooling) with different parameters as explained in Table 2. For our first Convolutional Block, we make a window of  $3 \times 3$  and convolve the image through kernels, where number of filters is set to 16 and these number of filters increases by incoming convolutional layers. The layer-by-layer visualization of weights is shown in Figure 3.

After the convolution layer, we then apply batch normalization. Batch normalization is a strategy for preparing deep neural networks that normalizes inputs to a layer for every scaled-down bunch. This settles the learning process and reduces data variation. Let us have a look on CNN layers that how they works individually.

#### 3.5.3. The Input Layers

In this layer, the tensor to reshape and then restructure the tensor is followed up by layers. In the Input arguments of this layer, the properties of the data that are used to define the argument of a function for sizing are the width, height, and a channel. For the proposed CNN, it is  $1024 \times 1024 \times 1$  and a 2D image with 1024 rows and 1024 columns, where 1 is the color channels representation.

#### 3.5.4. Convolutional Layer

The convolution layer contains at least one convolutional operation. For the first convolutional layer, the kernel size is  $3 \times 3$  with equal padding. The output tensor and the input tensor have the same width and height. The tensor flow will add zeros in the rows and columns to ensure the same size. Convolutional blocks indicate how many times the image is iterated over 4 layers in proposed study. Our convolutional layer output size is  $(N - m + 1) \times (N - m + 1)$ . The output of the  $l$ -th convolution layer, denoted as in [30], consists of feature maps. It is computed as shown in Equation (7):

$$C_i^{(l)} = B_i^{(l)} + \sum_{j=1}^{a_i^{(l-1)}} K_{i,j}^{(l-1)} \times C_i^{(l)} \quad (7)$$

where  $B_i^{(l)}$  is the bias matrix and the convolution filter or kernel of size  $a \times a$  that connects the  $j$ -th feature map in layer  $(l - 1)$  with the  $i$ -th feature map in the same layer. The output layer consists of feature maps. The first convolutional layer has input space. Our first convolutional block is  $3 \times 3$ , and the number of filters used is 16.

### 3.5.5. Batch Normalization Layer

Batch normalization layers are utilized among the convolution and the ReLU layers to normalize the information  $x_i$  by estimating the  $\mu_B$  and  $\sigma_B^2$  over a smaller batch size to accelerate CNN training and furthermore limit the affectability of the organization introduction. The standardized computations are defined in Equation (8) [68]:

$$\hat{x}_i = \frac{x_i - \mu_B}{\sigma_B^2 + e} \quad (8)$$

The normalized output of input instance is shown as  $\hat{x}_i$ , where  $i$  is the corresponding instance of data. After batch normalization, the ReLU activation function is applied, after which max-pooling is applied.

### 3.5.6. Max Pooling Layer

Max pooling computation is the next step. The pooling counting will reduce the addition of the data. In this stage, the module max-pooling2D with a size of  $3 \times 3$  and a stride of 2 is used. For a pooling layer, one can specify only the filter/kernel size ( $F$ ) and the strides ( $S$ ).

$$\text{Pooling Output dimension} = [(I - F) / S] + 1 \times D \quad (9)$$

There is no special parameter in the pooling layer, but it has two hyperparameters: *Filter*( $F$ ) and *Stride*( $S$ ). In general, if we have input dimensions of  $W_1 \times H_1 \times D_1$ , then [69]

$$W_2 = (W_1 - F) / S + 1 \quad (10)$$

The kernel or operational window is represented as  $W$ ; the window that is needed to compute, represented as  $W_1$ ; and the result is shown as  $W_2$ . The number of filters in the proposed CNN is changed in each block in the convolutional layers, where the max-pooling filter window size remains the same at  $2 \times 2$  with a stride of 1. The image is then downsampled to max-pooled data that are further processed by the subsequent layers.

$$H_2 = ((H_1 - F) / S + 1 - F) \quad (11)$$

In Equation (11),  $F$  is the spatial extent in the given filter of the image, and  $H$  is the height of the given image. These are the columns of the image. However, their height is calculated as stride by subtracting the assigned corresponding number of filters with their  $3 \times 3$  size. This is later on subtracted from the stride with a summation of 1 by subtracting it from the spatial extent.

$$D_2 = D_1 \quad (12)$$

If the volume of an input image is  $W_1 \times H_1 \times D_1$ , then an output of size  $W_1 \times H_1 \times D_1$  is produced by a pooling layer. The equations for  $W_2$ ,  $H_2$ , and  $D_2$  in the pooling layer are shown above, where  $W_2$ ,  $H_2$ , and  $D_2$  are the width, height, and depth of the output, respectively.

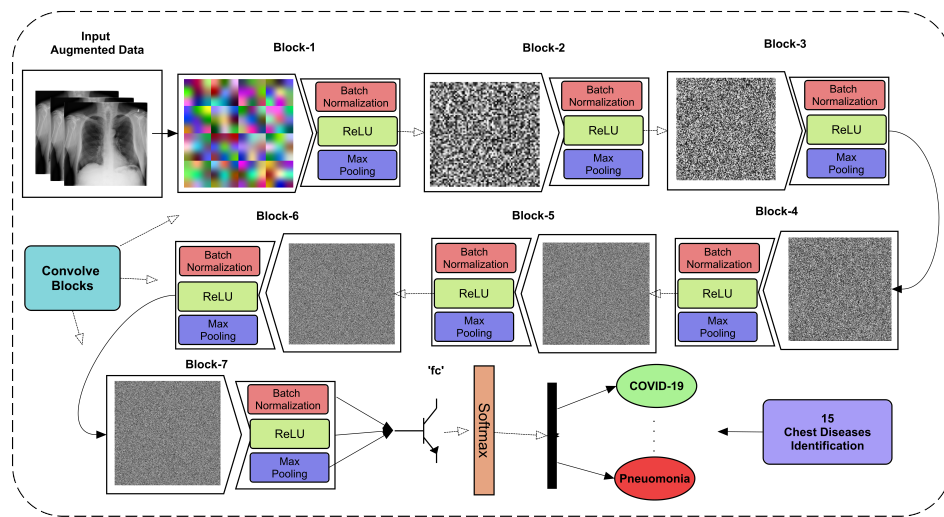


**Figure 3.** Proposed CNN design with convolve layer weight activation.

### 3.5.7. Rectified Linear Unit (ReLU)

ReLU refers to the Rectifier Unit, the most ordinarily conveyed initiation work for the output of CNN neurons. Unfortunately, ReLU work is not differentiable at the beginning, which makes it difficult to use with backpropagation preparation. In this layer, we eliminate low values from the sifted picture and supplant it with nothing. This capacity is possibly enacted when the hub input is over a specific amount. Thus, when the info is under zero, the yield is zero.

$$f(x) = \max(0, x) \text{ where } x = \text{input value} \quad (13)$$

Therefore, to cover any in-bounding and out-bounding range of pixels, the activation function is performed, and this normalizes incoming values. The summarizing details have been shown in Equation (13) [1].

### 3.5.8. Softmax Layer

Softmax is a numerical capacity that changes over a vector of numbers into a vector of probabilities, where the probabilities of each value correspond to the general size of each value in the vector. Convolutional layers are layers where channels are applied to the first picture, or to other element maps in a deep CNN. We use 32 layers for training. The table of CNN layers (Table 3) is given below.

**Table 3.** Details about the proposed CNN layers.

Number	Layer Names	Activations	Kernel Size	Stride	Parameters	Feature Maps
1	Input layer	$1024 \times 1024 \times 3$	/	$1024 \times 1024$	/	/
2	Convolutional layer (C1)	$1024 \times 1024 \times 3$	$3 \times 3$	1	Weights = $3 \times 3 \times 3 \times 16$ Bias = $1 \times 1 \times 16$	16
3	Batch Normalization (BN1)	$1024 \times 1024 \times 16$	/	/	Offset = $1 \times 1 \times 16$ Scale = $1 \times 1 \times 16$	16
4	ReLU (R1)	$1024 \times 1024 \times 16$	/	/	/	/
5	Maximum pooling layer (MP1)	$1024 \times 1024 \times 16$	$2 \times 2$	2	/	/

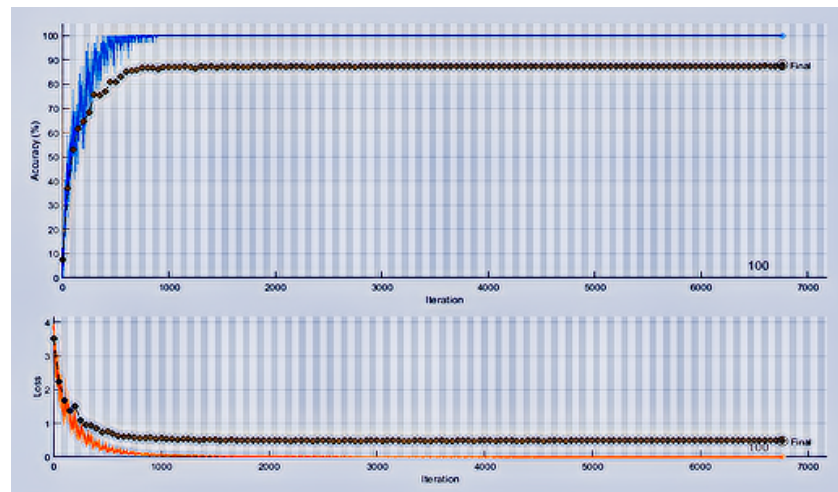
**Table 3.** Cont.

Number	Layer Names	Activations	Kernel Size	Stride	Parameters	Feature Maps
6	Convolutional layer (C2)	$512 \times 512 \times 16$	$3 \times 3$	1	Weights = $3 \times 3 \times 16 \times 32$ Bias = $1 \times 1 \times 32$	32
7	Batch Normalization (BN2)	$512 \times 512 \times 32$	/	/	Offset = $1 \times 1 \times 32$ Scale = $1 \times 1 \times 32$	32
8	ReLU (R2)	$512 \times 512 \times 32$	/	/	/	/
9	Maximum pooling layer (MP2)	$256 \times 256 \times 32$	$2 \times 2$	2	/	/
10	Convolutional layer (C3)	$256 \times 256 \times 64$	$3 \times 3$	1	Weights = $3 \times 3 \times 32 \times 64$ Bias = $1 \times 1 \times 64$	64
11	Batch Normalization (BN3)	$256 \times 256 \times 64$	/	/	Offset = $1 \times 1 \times 32$ Scale = $1 \times 1 \times 32$	64
12	ReLU (R3)	$256 \times 256 \times 64$	/	/	/	/
13	Maximum pooling layer (MP3)	$128 \times 128 \times 64$	$2 \times 2$	2	/	/
14	Convolutional layer (C4)	$128 \times 128 \times 128$	$3 \times 3$	1	Weights = $3 \times 3 \times 64 \times 128$ Bias = $1 \times 1 \times 128$	128
15	Batch Normalization (BN4)	$128 \times 128 \times 128$	/	/	Offset = $1 \times 1 \times 128$ Scale = $1 \times 1 \times 128$	128
16	ReLU (R4)	$128 \times 128 \times 128$	/	/	/	/
17	Maximum pooling layer (MP5)	$64 \times 64 \times 128$	$2 \times 2$	2	/	/
18	Convolutional layer (C5)	$64 \times 64 \times 256$	$3 \times 3$	1	Weights = $3 \times 3 \times 128 \times 256$ Bias = $1 \times 1 \times 256$	256
19	Batch Normalization (BN5)	$64 \times 64 \times 256$	/	/	Offset = $1 \times 1 \times 256$ Scale = $1 \times 1 \times 256$	256
20	ReLU (R5)	$64 \times 64 \times 256$	/	/	/	/
21	Maximum pooling layer (MP5)	$32 \times 32 \times 256$	$2 \times 2$	2	/	/
22	Convolutional layer (C6)	$32 \times 32 \times 512$	$3 \times 3$	1	Weights = $3 \times 3 \times 256 \times 512$ Bias = $1 \times 1 \times 512$	512
23	Batch Normalization (BN6)	$32 \times 32 \times 512$	/	/	Offset = $1 \times 1 \times 512$ Scale = $1 \times 1 \times 512$	512
24	ReLU (R6)	$32 \times 32 \times 512$	/	/	/	/

**Table 3.** Cont.

Number	Layer Names	Activations	Kernel Size	Stride	Parameters	Feature Maps
25	Maximum pooling layer (MP6)	$16 \times 16 \times 512$	$2 \times 2$	2	/	/
26	Convolutional layer (C7)	$16 \times 16 \times 1024$	$3 \times 3$	1	Weights = $3 \times 3 \times 512 \times 1024$ Bias = $1 \times 1 \times 1024$	1024
27	Batch Normalization (BN7)	$16 \times 16 \times 1024$	/	/	Offset = $1 \times 1 \times 1024$ Scale = $1 \times 1 \times 1024$	1024
28	ReLU (R7)	$16 \times 16 \times 1024$	/	/	/	/
29	Maximum pooling layer (MP7)	$8 \times 8 \times 1024$	$2 \times 2$	2	/	/
30	Fully connected layer FC1	$1 \times 1 \times 15$	/	/	Weights = $15 \times 65,536$ Bias = $15 \times 1$	15
31	Softmax	$1 \times 1 \times 15$	/	/	/	/
32	Classification Layer	/	/	/	/	/

Table 3 shows the fine-tuned CNN details for 15 categories of chest disease detection, where padding, stride, and other fine details of CNN show how the fine features are being collected and passed on to the next block. There are seven total Conv-Blocks in which a 4-layer combination is used by conducting a downsample of half of the size, as compared to the previous layer input. A training and validation graph of the proposed CNN is shown in Figure 4, where the consistent confidence of validation accuracy is shown. However, the accuracy graph is saturated over a few epochs. Various approaches using hyperparameters optimization, such as changing the learning rate (LR), the activation function, and epochs, are considered. Finely, the fine-tuned parameters for case study are shown in Table 4.

**Figure 4.** CNN training graph.

**Table 4.** The fine-tuned parameters of the proposed CNN.

Parameter	Value
Stochastic gradient descent momentum (SGDM)	0.9
Learning Rate (LR)	0.0004
Verbose	No
Max-epochs	500
Iteration-Frequency	65
Min-Batch Size	32

As discussed above, the training parameters of the proposed CNN are shown in Table 4. It is observed that max-epochs are taken as 500, which are manually stopped due to the saturation of change in validation accuracy. The initial learning rate is set to 0.0004, where the frequency of iteration is taken as 65. Considering 13,000 iterations in total, by looking into a consistent accuracy rate from 1000 to more than 6000, training was manually stopped after 6764 iterations. At this time, epochs reached 105. After obtaining poor results of classification on validation and testing data, the state-of-the-art deep features using self-activations of CNN are applied. The self-activations are referred to as no other pre-trained model is used to extract deep features where the proposed CNN based transfer learning is performed on its fully-connected layer.

### 3.6. ML-Based Classification

Many of the state-of-the-art machine learning classifiers are used when a comparison of algorithm performance is proposed. Support Vector Machine (SVM) is an algorithm used for linearity in data. We consider training features and training labels. Training labels are already defined, and every machine learning or SVM classifier selects the numeric value row by row from the table, so this training features results as  $2100 \times 15$  feature vector, which means 2100 rows in every single image, as we have 2100 images for training and 15 is the number of features. Basically, in this, we design a matrix that consists of rows and columns. As we know, the rows are a feature, so there are n columns in front of every row, and this is a feature vector of a single image. Testing is performed using testing features that are performed on a trained model. The predictions function is performed, and we map these predicted labels on testing labels and calculate the accuracy, which is maximally reached to 99.98%. The testing features data contain a  $900 \times 15$  size vector array where 900 is representing to testing features instances and 15 is the number of features. Different evaluation measures are used for evaluation on multiple trained model predictions. The all testing measures are discussed in Section 4.

### 3.7. Deep Features Extraction

Transfer learning is an examination issue in AI that emphasizes putting acquired information away while tackling an issue and applying it to another related issue. For instance, information acquired while figuring out how to perceive vehicles can be applied when attempting to perceive trucks. Basically, we train our CNN mainly with 106 epochs. In our train network we take preprocessed Training data. First, we consider two datasets—the NIH Chest X-ray Dataset and the COVID-19 Chest X-ray Image Dataset, perform a process of normalization on them, and change the scale. We then make the image sizes of both datasets the same. After the normalization process, a dataset with a normalization form of 200 images of 15 different diseases is created. Our proposed CNN achieved validation accuracy that is 87.89% in 105 epochs with 6764 iterations. We also checked the 105 epochs with 13,000 iterations, but the result was the same. In the training graph, the Black Dots are Validation data. To check the accuracy, we load the model, but the

accuracy is in two forms: (1) the model and (2) validation accuracy. This takes a very long time and an extensive validation process, but the accuracy is still very low, at 87.89%. Therefore, we utilize our proposed CNN fully-connected layer to obtain deep features and perform a machine learning classification process such as SVM or decision tree using 10-fold and 5-fold validation methods where accuracy reaches 95, 98, and 99%. We use the machine learning process because it is highly time-efficient as compared to deep learning. We perform the activations on CNN using fully-connected layer, in which there are 15 classes. These activations get training features on our training data and testing features on testing data.

#### 4. Results and Discussions

With the use of the two best datasets, the CNN and the activation of CNN provides machine learning techniques with fivefold and tenfold validation techniques included in the proposed work. We show the result of the proposed work in the form of tables and graphs where the training set is utilized to prepare the model, while the validation set is simply used to assess the model's presentation. We made a table of CNN activation for the tenfold technique and calculated the individual accuracy of individual classes. In Tables 3 and 4, detailed CNN layers and training parameters are shown. CNN validation accuracy as shown in Figure 4 remains saturated with an 87.89% validation accuracy.

The results of CNN testing data are further discussed for each class that increase the testing accuracy as compared to validation accuracy. Furthermore, other important evaluation measure are also use and shown in Table 5.

**Table 5.** CNN testing data results.

Classes	Accuracy (%)	Sensitivity (%)	Specificity (%)	F1-Score (%)	Precision (%)	Kappa (%)
Atelectasis	0.96667	0.96667	0.99524	0.95082	0.93548	0.86492
Cardiomegaly	1	1	1	1	1	0.86667
Consolidation	1	1	1	1	1	0.86667
Covid-19	0.93333	0.93333	0.99524	0.93333	0.93333	0.8673
Edema	1	1	1	1	1	0.86667
Effusion	0.9	0.9	0.99286	0.9	0.9	0.86761
Emphysema	0.96667	0.96667	0.99762	0.96667	0.96667	0.86698
Fibrosis	0.96667	0.96667	1	0.98305	1	0.86904
Hernia	1	1	1	1	1	0.86667
Infiltration	0.96667	0.96667	0.99762	0.96667	0.96667	0.86698
Mass	1	1	0.99762	0.98361	0.96774	0.8646
Nodule	0.93333	0.93333	0.99762	0.94915	0.96552	0.86935
Pleural Thickening	1	1	0.99762	0.98361	0.96774	0.8646
Pneumonia	0.96667	0.96667	1	0.98305	1	0.86904
Pneumothorax	0.9	0.9	0.99286	0.9	0.9	0.86761
Overall	0.9667	0.9667	0.9976	0.9667	0.9669	0.7321

Although the validation accuracy was lower when testing data were collected at a 70:15:15 ratio: 70% data is used as training data, 15% as validation, and 15% as testing data, the overall results of classification are improved. The F1-score is an important measure

of evaluation as it contains the effect of precision and recall. The precision is the ratio of true positives over true positives and false positives. The 96.67% value is a good measure of predictivity. Similarly, a kappa value of more than 60% shows the moderate level of agreement on testing data. However, to increase the overall evaluation measure performance, the transfer learning based deep features are used and tested via classical machine learning methods that improved the accuracy and other results as well.

Although the CNN testing data results were good enough, to increase accuracy, the transfer learning concept was used. Therefore, to improve the testing data results, deep transfer learning is utilized using self-activation on the proposed trained fully connected CNN layers. These features are embedded within classical ML classification methods. The best classification results selected among 23 different methods are shown in Tables 6 and 7 with fivefold and tenfold validation methods.

**Table 6.** Classification validation accuracy of fivefold validation using self-activated features.

Method	Accuracy (%)	Sensitivity (%)	Specificity (%)	F1-Score (%)	Precision (%)	Kappa (%)
Bag-Ensemble	99.33	99.33	99.95	99.33	99.34	96.64
KNN-coarse	96.17	96.17	99.73	96.17	96.23	69.20
KNN-fine	99.40	99.40	99.96	99.40	99.41	95.18
KNN-medium	96.30	96.30	99.74	96.30	96.34	70.27
LP-Boost-Ensemble	99.1	99.10	99.94	99.10	99.12	92.77
Subspace-discriminant	93.40	93.40	99.53	93.44	93.55	46.96
Total-boost-Ensemble	99.17	99.17	99.94	99.17	99.18	93.30

K-fold cross-validation is a technique that endeavors to expand the utilization of accessible information for training and afterward testing a model. It is especially valuable for surveying model execution, as it gives a scope of accuracy scores across (to some degree) different datasets. K-fold CV is a method where a given informational index is part of a K number of segments/folds, where each fold is eventually utilized as a testing set. Let us consider the situation of fivefold cross-validation ( $K = 5$ ). This cycle is repeated until each of the five folds has been utilized as the testing set. The validation accuracy using fivefold validation means that it makes five folds of all the input data from which the randomized instances are selected in each fold. Afterwards, one fold is trained and tested on the four other folds, where results are saved as one-fold predictions. Similarly, two folds selected for training and testing are performed on three folds, and the results of the predictions are saved. At last, when all folds' training and testing is performed, the mean of all predicting results is taken and shown as fivefold prediction results. By doing these cross-fold validation methods, the biases in predicting and training decreases almost to zero. Therefore, the proposed study uses these five- and tenfold methods to make the proposed results more promising. In Table 6, we can see almost all methods perform more than 99% of the results, except for the KNN-coarse, KNN-medium, and subspace-discriminant methods. The other results of these methods in terms of sensitivity, specificity, precision, F1-score, and the statistical method of evaluation (kappa-cohen) index are used. Generally, the validation accuracy is the ratio between the summation of true positives, true negatives with the summation of true positives, true negatives, false positives, and false negatives. This tells us how many true results for positive and negative classes are found. The evaluation measures operational calculations are shown in Equations (14)–(19) [70].

$$Accuracy = \frac{(TP + TN)}{(TP + FN) + (FP + TN)} \quad (14)$$

In the proposed study, there are 15 classes, so it is not about two classes. It considers the multi-class problem validation accuracy.

$$Sensitivity = \frac{(TP)}{(TP + FN)} \quad (15)$$

The other measure called recall or sensitivity is used to measure true positivity predictions among actual true positives.

$$Specificity = \frac{(TN)}{(FP + TN)} \quad (16)$$

The specificity measure is used to measure the true negatives among actual negatives. The precision is similar to sensitivity, which is used to measure over the summation of true negatives and false negatives; precision is used to measure the summation of true positives and false positives. However, the proposed studies used both to cross check the true positive predictions.

$$Precision = \frac{(TP)}{(TP + FN)} \quad (17)$$

The F1-score is used to measure the ratio of the product of precision and recall with the summation of precision and recall. Sometimes, the true positivity and true negativity predictions may lead to incorrect perceptions due to data imbalancing. Therefore, we need to give weights to false positives and false negatives for the mean measurement.

$$F1-Score = \frac{2 \times (TP)}{(2 \times TP + FN + FP)} \quad (18)$$

Similarly, a statistical evaluation measure calculated from a confusion matrix of predicted data also uses four evaluation measures to give a confidence value. Its confidence range changes from 50 to 90+, where the 90+ value yields strong confidence, where 0–20% = None, 21–39% = Minimal, 40–59% = Weak, 60–79% = Moderate, 80–90% = Strong, and Above 90% = an almost Perfect Confidence in the proposed model of classification.

$$Agreement_{level} = \frac{\left( \frac{x_{cm} \times x_{rm}}{n} \right) + \left( \frac{y_{cm} \times y_{rm}}{n} \right)}{n} \quad (19)$$

In Equation (19),  $x$  is a cm and rm value showing the column 1 and the row 1 predicted values of the confusion matrix, and  $y$  is a cm and rm value showing the column 2 and the row 2 value of the confusion matrix for two classes only where in the proposed study, which uses 15 classes that indicate a 15 cm and rm value from both  $x$  and  $y$  aspects.

In Table 6, we can see that there are seven different classification models used, where four of them yield 99%+ accuracies. The bag-ensemble, KNN-fine, the LP-boost ensemble, and total-boost yield 99.33%, 99.40%, 99.1%, and 99.17% validation accuracies, respectively. It is further noticed that accuracy, sensitivity, and precision values remain the same. Therefore, we can say that the true positivity predictions over the true negatives and false negatives do not affect it. However, multiple evaluation measure usage covers it by evaluating the results in a different way. The F1-score uses both precision and sensitivity, which yields 99.33% again using the bag-ensemble method, as in the other six methods used in this study. The specificity calculated over the true negatives that changes for all methods is used in Table 6. It remains higher than the sensitivity values in all methods. However, we can say that the true negative predictions are more accurate than the true positive predictions. The changed precision value, as compared to sensitivity, includes the sum of TP and FP in the denominator over the precision values, which shows slightly higher values as compared to validation accuracy. This shows that the true positive predictions outnumber the false positives.

The statistical measure covers each aspect of the TP, FP, NP, and TN values to yield a confidence value. It can be observed that KNN-Fine has the highest accuracy, but the kappa index is not higher. The highest kappa value is of the bag-ensemble method with 96.64%, which makes it the best over all methods of classification. To cross-validate and remove bias, if any, more folding methods can validate it. The tenfold validation method is also used and shown in Table 7.

**Table 7.** Classification validation accuracy of tenfold validation using self-activated features.

Method	Accuracy (%)	Sensitivity (%)	Specificity (%)	F1-Score (%)	Precision (%)	Kappa (%)
Bag-Ensemble	99.77	99.77	99.98	99.73	99.74	97.86
KNN-coarse	96.20	96.20	99.73	96.20	96.26	69.46
KNN-fine	99.67	99.67	99.98	99.67	99.67	97.32
KNN-medium	96.37	96.37	99.74	96.37	96.41	70.80
LP-Boost-Ensemble	99.47	96.47	99.96	99.47	99.48	95.71
Subspace-discriminate	96.53	96.53	99.75	96.53	96.56	72.14
Total-boost-Ensemble	99.63	99.63	99.97	99.63	99.64	97.05

The same classification methods are used with the ten-fold cross validation method. The results are slightly higher than the fivefold method results. The validation accuracy for the bag-ensemble method increased from 99.33% to 99.77%. Similarly, it increased the validation accuracy results for other lower-value algorithms as well. Therefore, we can say that the proposed method is more promising because it uses more randomized folding, which is good for big data usage as well. By increasing validation accuracy, the other two values—sensitivity and F1-score—remain the same, except the specificity of bag-ensemble, which decreased from 99.77 to 99.73%. The specificity remains above 99% in both five- and tenfold methods, where it increased in decimal values in the case of the tenfold method. The Kappa Cohen index overall in all methods increases its confidence on the predicted results of each algorithm.

The best kappa value method in the fivefold method was bag-ensemble, with 96.64%, which was increased to 97.86% in the tenfold method. The 2nd best kappa value in the fivefold method was 95.18% for KNN-fine, which is also increased to 97.32%. The 3rd and 4th best kappa value for LP-boost and total boost was 92.77% and 93.30%, respectively, and are increased from 92.37% to 95.71% and from 93.30% to 97.05% for both methods. The increasing results in all evaluation measures for the tenfold method makes the proposed results more promising for chest disease identification.

We here provide a table of CNN activations of the five-fold technique and calculate the individual accuracy for each class. The results are shown in Table 8.

The individual disease detection rate will lead us to propose a more confident model for particular disease detection. COVID-19 needs to be detected quickly and cheaply. In the proposed study, using the fivefold validation method showed that the best kappa value in the COVID-19 detection results was 99.0, i.e., the bag-ensemble. Similarly, for the other algorithms, i.e., the KNN-fine, LP-boost, and total-boost methods, the COVID-19 classification accuracy was 100%, 100%, and 98.0%, respectively. This shows that COVID-19 disease detection is highly accurate using the proposed framework. The COVID-19 results are set as a point of reference for investigating other chest disease detection results. Most of the results were detected with 100% or 99% accuracy. The best kappa value was attained with the bag-ensemble method. The all-class results were either 99% accurate or 100% accurate, but the Atelectasis disease classification was 97% accurate.

**Table 8.** Self-activated features based on classification using the fivefold technique results on individual class accuracy.

Classes	Bag-Ensemble	KNN-Coarse	KNN-Fine	KNN-Medium	LP-Boost Ensemble	Subspace-Discriminant	Total-Boost Ensemble
Atelectasis	97.00	95.0	99.0	94.0	100	88.0	97.0
Cardiomegaly	100	99.0	100	99.95	99.0	99.0	99.0
Consolidation	99.0	97.0	100	97.0	99.0	94.0	100
COVID-19	99.0	96.0	100	97.5	100	90.0	98.0
Edema	99.0	97.50	99.0	98.0	100	97.0	100
Effusion	100	89.0	100	90.0	100	89.0	97.0
Emphysema	100	96.0	98.0	99.6	100	95.0	98.50
Fibrosis	99.0	99.0	99.0	98.0	99.0	98.0	100
Hernia	100	100	100	100	100	100	100
Infiltration	100	96.0	100	96.0	100	94.0	100
Mass	99.0	97.0	100	97.0	99.0	89.0	100
Nodule	100	94.0	99.0	95.0	97.0	88.0	100
Pleural Thickening	100	99.0	100	99.0	99.0	92.0	100
Pneumonia	99.0	99.0	99.0	99.0	98.0	100	100
Pneumothorax	99.0	89.0	98.0	88.5	96.50	88.0	98

Similarly, the KNN-fine method was 100% accurate in COVID-19 detection, and Atelectasis detection accuracy was increased, as compared to the bag-ensemble method (97% to 99%). Emphysema, nodule, and pneumothorax disease results decreased from 100 to 98%, from 100 to 99%, and from 99 to 98%, respectively. The third best model in the fivefold method was the LP-boost method, which also achieves 100% COVID-19 detection results, where the Atelectasis disease results, as compared to the bag-ensemble method, increased from 97% to 100%. However, other classification results decreased slightly. For example, for Cardiomegaly, it decreased from 100 to 99%; for Nodule, it decreased from 100 to 97%; for Pleural Thickening, it decreased from 100 to 99%; and for pneumothorax, it decreased from 99 to 96.50%. However, it not only decreased the detection rate, but also increased in other disease detection results. The fourth best model, the total boost, also detected COVID-19 with 98% accuracy. It also decreased the classification results of Effusion, Emphysema, and Pneumothorax. In other disease detection results, it increased the detection rate, but it maintained results for some diseases. However, by looking into all ML classification methods, all performances are promising using the proposed method for multi-class chest disease detection. The ten-fold validation method proved to be more accurate than the fivefold method. This method based on individual class detection results are shown in Table 9.

We can see in Table 9 that the COVID-19 detection accuracies achieved by the best algorithms showed 100%, 99%, 99%, and 99% for the bag-ensemble, KNN-fine, LP-boost, and total boost methods, respectively. We can set the bag-ensemble algorithm results as a frame of reference for disease detection. The other algorithms showed that other methods are 1% less accurate than the bag-ensemble method. This method also achieves the highest confidence value of kappa. This algorithm not only achieves 100% for COVID-19 detection but also increases the classification accuracy for Atelectasis to 99%, which was 97% in the fivefold method. Furthermore, it also increased the detection results for fibrosis, mass, pneumonia, and pneumothorax from 99% to 100%. However, it decreased

detection of infiltration from 100% to 98%. This disease detection decrease is negligible if we look upon the improvement of the other six diseases. However, the best results achieved by the tenfold method makes the detection rate of all diseases 100%, except for three, two of which (Atelectasis and Consolidation) are 99% accurate and one is 98% (Infiltration). Furthermore, the 2nd best method also improved the results of detection for all diseases. It ranges from 99 to 100%. The 10 classes reach 100% (cardiomegaly, consolidation, edema, emphysema, fibrosis, hernia, mass, nodule, pleural thickening, and pneumonia) accuracy, where five (atelectasis, COVID-19, effusion, infiltration, and pneumothorax) reach 99%, so these results are improved compared to the fivefold validation approach. The 3<sup>rd</sup> best model, LP-boost, also increases its detection results and reaches 100 detections in eight diseases (cardiomegaly, edema, fibrosis, hernia, infiltration, mass, nodule, and pleural-thickening), 99% for five diseases (atelectasis, consolidation, COVID-19, pneumonia, and pneumothorax), and 98% for two diseases (effusion and emphysema). The 4<sup>th</sup> best model also improved its results by giving a 100% accurate detection for nine diseases (cardiomegaly, consolidation, edema, emphysema, fibrosis, hernia, infiltration, pleural thickening, and pneumonia) and 99% for six other diseases (atelectasis, COVID-19, effusion, mass, nodule, and pneumothorax).

**Table 9.** Self-activated features based on classification using the ten-fold technique results on individual class accuracy.

Classes	Bag-Ensemble	KNN-Coarse	KNN-Fine	KNN-Medium	LP-Boost Ensemble	Subspace-Discriminant	Total-Boost Ensemble
Atelectasis	99	95	99	94	99	91	99
Cardiomegaly	100	99	100	99	100	98	100
Consolidation	99	97	100	97	99	96	100
COVID-19	100	96	99	98	99	93	99
Edema	100	97	100	98	100	98	100
Effusion	100	90	99	9	98	95	99
Emphysema	100	96	100	96	98	99	100
Fibrosis	100	99	100	99	100	99	100
Hernia	100	100	100	100	100	100	100
Infiltration	98	96	99	96	100	96	100
Mass	100	97	100	97	100	98	99
Nodule	100	94	100	95	100	93	99
PleuralThickening	100	99	100	99	100	98	100
Pneumonia	100	99	100	99	99	100	100
pneumothorax	100	89	99	88	99	94	99

It is observed that the tenfold method shows the less accurate results. The kappa confidence value is improved in the tenfold method. Therefore, tenfold cross-validation is a more robust, confident, promising method to classify chest diseases using more randomization and folds. The comparison of state-of-the-art studies on COVID-19 disease detection and other chest diseases are shown in the next section.

#### *Comparison of with Previous Studies*

The proposed study was used to solve multi-class classification problem for chest diseases. Few studies cover the multiple aspects of chest diseases, but currently, the problem must include COVID-19 among chest diseases. By including COVID-19, the proposed

method not only solved the other single-class chest disease detection problems, but also covered the COVID-19 single-class detection studies. The comparison with state-of-the-art recent methods is summarized in Table 10.

**Table 10.** Existing method comparison.

Sr. No.	Title of the Paper	Authors Names	Classifiers Used	Accuracy Achieved
1	Disease Staging and Prognosis in Smokers Using Deep Learning	Samuel Yash et al.	CNN	74.95%
2	Deep Learning for Screening COVID-19	Sanhita Basu et al.	(DL) (ML)	90.13%
3	A Deep Neural Network to distinguish COVID-19...	Saleh Albahli et al.	CNN	87%
4	Chest CT manifestations of new coronavirus	Zheng ye et al.	GGO	98%
5	Chest CT Findings in Coronavirus Disease-19...	Adam Brenham et al.	Ct scan	88%
6	Chest pathogens detection using deep learning	Y bar et al.	Deep learning	87–94%
7	Chest disease radiography in two-fold	Prakash et al.	CNN	97%
8	Pneumonia Detection on Chest X-Ra	Tej Bahadur Chandra et al.	ML	95.8%
9	Proposed	Proposed	CNN, ML	KNN = 99.8% Boosted trees = 99.6 Subspace KNN = 99.7%

Table 10 shows the comparison of the proposed models with various studies of ML- and DL-based methods. The 1st comparison shows the staging problem solver for smokers' diseases and achieves up to 74.95% accuracy. The 2nd comparison shows that the DL-based COVID-19 detection results reach 90.13%. The 3rd comparison used a DL method and achieved 87%. The 4th comparison shows that the chest CT scan-based analysis of the GGO classifier achieve 98% accuracy. Another chest detection method showed 87.94%. The 7th comparison showed 97% using the radiographical method and a modality of images for chest disease detection. The last comparison used X-ray modality using ML classification methods and achieved 95.8%. The proposed study finally shows more accurate results on all compared studies. There are many other studies that focus either on a single disease of pneumonia, COVID-19, or some other chest disease, but most studies do not cover the multi-class problem in order to classify chest studies.

## 5. Conclusions

The proposed study uses a combined dataset of X-ray modality for chest disease detection by including a COVID-19 X-ray imaging dataset. To normalize the data, data augmentation is performed. This preprocessed data removes data bias, if there is any. However, a novel CNN is proposed for multi-chest disease detection. It saturates its learning in its training time by reporting an 87.89% validation accuracy. To increase the prediction results and reduce the prediction time, deep transfer learning is applied. In this way, self-activated deep features are extracted from the fully-connected layer of the proposed CNN. The deep features are fed to seven different domain algorithms of the ML approach. To make the proposed study more promising, two methods of validation (5- and 10-fold) are performed. It is observed from the results that more folding makes the results more accurate. This means that the proposed study can be used to detect multi-class chest

disease detection. It not only increases accuracy, but also reduces the prediction time of a given testing sample. At last, a comparison shows the improvement of the proposed study from either single-class chest diseases or multi-class chest diseases, including COVID-19.

In the future, multi-class decision-making CAD systems in different aspects of the medical domain should be used. However, data normalization needs to be considered to make the data reliable. Big data samples are encouraged for more confident results of chest diseases. The deep transfer learning features are also encouraged.

**Author Contributions:** Conceptualization, N.-u.R., M.S.Z., T.M., H.T.R., and R.D.; Funding acquisition, A.M.E.-S. and M.A.E.-M.; Methodology, N.-u.R. and M.S.Z., T.M., H.T.R., R.D., A.M.E.-S., and M.A.E.-M.; Software, N.-u.R., M.S.Z., T.M., H.T.R., R.D., A.M.E.-S., and M.A.E.-M.; Visualization, H.T.R.; Writing—original draft, N.-u.R., M.S.Z., T.M., H.T.R., R.D., A.M.E.-S., and M.A.E.-M.; Supervision, H.T.R. and R.D. All authors have read and agreed to the published version of the manuscript.

**Funding:** The authors extend their appreciation to King Saud University for funding this work through Researcher Supporting Project (RSP- 2021/133), King Saud University, Riyadh, Saudi Arabia.

**Institutional Review Board Statement:** Not applicable.

**Informed Consent Statement:** Not applicable.

**Data Availability Statement:** Not applicable.

**Conflicts of Interest:** The authors declare no conflicts of interest.

## References

1. Er, O.; Yumusak, N.; Temurtas, F. Diagnosis of chest diseases using artificial immune system. *Expert Syst. Appl.* **2012**, *39*, 1862–1868. [[CrossRef](#)]
2. Schluger, N.W.; Koppaka, R. Lung Disease in a Global Context. A Call for Public Health Action. *Ann. Am. Thorac. Soc.* **2014**, *11*, 407–416. [[CrossRef](#)] [[PubMed](#)]
3. Jaiswal, A.K.; Tiwari, P.; Kumar, S.; Gupta, D.; Khanna, A.; Rodrigues, J.J. Identifying pneumonia in chest X-rays: A deep learning approach. *Measurement* **2019**, *145*, 511–518. [[CrossRef](#)]
4. Lambrecht, B.N.; Hammad, H. The immunology of asthma. *Nat. Immunol.* **2015**, *16*, 45–56. [[CrossRef](#)] [[PubMed](#)]
5. Sudre, P.; Ten Dam, G.; Kochi, A. Tuberculosis: A global overview of the situation today. *Bull. World Health Organ.* **1992**, *70*, 149. [[PubMed](#)]
6. Bando, H.; Nishio, T.; Bamba, H.; Uno, T.; Hisa, Y. Vocal fold paralysis as a sign of chest diseases: A 15-year retrospective study. *World J. Surg.* **2006**, *30*, 293–298. [[CrossRef](#)]
7. Kong, W.; Agarwal, P.P. Chest imaging appearance of COVID-19 infection. *Radiol. Cardiothorac. Imaging* **2020**, *2*, e200028. [[CrossRef](#)]
8. Jacobi, A.; Chung, M.; Bernheim, A.; Eber, C. Portable chest X-ray in coronavirus disease-19 (COVID-19): A pictorial review. *Clin. Imaging* **2020**, *64*, 35–42. [[CrossRef](#)]
9. Steffens, I. A hundred days into the coronavirus disease (COVID-19) pandemic. *Eurosurveillance* **2020**, *25*, 2000550. [[CrossRef](#)]
10. Filho, P.P.R.; Barros, A.C.S.; Ramalho, G.L.B.; Pereira, C.R.; Papa, J.P.; de Albuquerque, V.H.C.; Tavares, J.M.R.S. Automated recognition of lung diseases in CT images based on the optimum-path forest classifier. *Neural Comput. Appl.* **2019**, *31*, 901–914. [[CrossRef](#)]
11. Da Nóbrega, R.V.M.; Rebouças Filho, P.P.; Rodrigues, M.B.; da Silva, S.P.P.; Dourado Júnior, C.M.J.M.; de Albuquerque, V.H.C. Lung nodule malignancy classification in chest computed tomography images using transfer learning and convolutional neural networks. *Neural Comput. Appl.* **2020**, *32*, 11065–11082. [[CrossRef](#)]
12. Elaziz, M.A.; Ewees, A.A.; Yousri, D.; Alwerfali, H.S.N.; Awad, Q.A.; Lu, S.; Al-Qaness, M.A.A. An Improved Marine Predators Algorithm with Fuzzy Entropy for Multi-Level Thresholding: Real World Example of COVID-19 CT Image Segmentation. *IEEE Access* **2020**, *8*, 125306–125330. [[CrossRef](#)] [[PubMed](#)]
13. Khan, M.A.; Rubab, S.; Kashif, A.; Sharif, M.I.; Muhammad, N.; Shah, J.H.; Zhang, Y.; Satapathy, S.C. Lungs cancer classification from CT images: An integrated design of contrast based classical features fusion and selection. *Pattern Recognit. Lett.* **2020**, *129*, 77–85. [[CrossRef](#)]
14. Sahlol, A.T.; Elaziz, M.A.; Jamal, A.T.; Damaševičius, R.; Hassan, O.F. A novel method for detection of tuberculosis in chest radiographs using artificial ecosystem-based optimisation of deep neural network features. *Symmetry* **2020**, *12*, 1146. [[CrossRef](#)]
15. Sahlol, A.T.; Yousri, D.; Ewees, A.A.; Al-qaness, M.A.A.; Damasevicius, R.; Elaziz, M.A. COVID-19 image classification using deep features and fractional-order marine predators algorithm. *Sci. Rep.* **2020**, *10*, 15364. [[CrossRef](#)] [[PubMed](#)]
16. Chandra, T.B.; Verma, K. Analysis of quantum noise-reducing filters on chest X-ray images: A review. *Meas. J. Int. Meas. Confed.* **2020**, *153*, 107426. [[CrossRef](#)]

17. Yahyaoui, A.; Yumuşak, N. *Decision Support System Based on the Support Vector Machines and the Adaptive Support Vector Machines Algorithm for Solving Chest Disease Diagnosis Problems*; Springer Nature: Basingstoke, UK, 2018.
18. Roberts, M.; Driggs, D.; Thorpe, M.; Gilbey, J.; Yeung, M.; Ursprung, S.; Aviles-Rivero, A.I.; Etmann, C.; McCague, C.; Beer, L.; et al. Common pitfalls and recommendations for using machine learning to detect and prognosticate for COVID-19 using chest radiographs and CT scans. *Nat. Mach. Intell.* **2021**, *3*, 199–217. [[CrossRef](#)]
19. Kumar, N.M.; Mohammed, M.A.; Abdulkareem, K.H.; Damasevicius, R.; Mostafa, S.A.; Maashi, M.S.; Chopra, S.S. Artificial intelligence-based solution for sorting COVID related medical waste streams and supporting data-driven decisions for smart circular economy practice. *Process Saf. Environ. Prot.* **2021**, *152*, 482–494. [[CrossRef](#)]
20. Kumar, V.; Singh, D.; Kaur, M.; Damaševičius, R. Overview of Current State of Research on the Application of Artificial Intelligence Techniques for COVID-19. *PeerJ Comput. Sci.* **2021**, *7*, e564. [[CrossRef](#)]
21. Jordan, M.I.; Mitchell, T.M. Machine learning: Trends, perspectives, and prospects. *Science* **2015**, *349*, 255–260. [[CrossRef](#)]
22. Alom, M.Z.; Taha, T.M.; Yakopcic, C.; Westberg, S.; Sidike, P.; Nasrin, M.S.; Hasan, M.; Van Essen, B.C.; Awwal, A.A.S.; Asari, V.K. A state-of-the-art survey on deep learning theory and architectures. *Electronics* **2019**, *8*, 292. [[CrossRef](#)]
23. Bai, X.; Wang, X.; Liu, X.; Liu, Q.; Song, J.; Sebe, N.; Kim, B. Explainable deep learning for efficient and robust pattern recognition: A survey of recent developments. *Pattern Recognit.* **2021**, *120*, 108102. [[CrossRef](#)]
24. Saba, L.; Biswas, M.; Kuppili, V.; Cuadrado Godia, E.; Suri, H.S.; Edla, D.R.; Omerzu, T.; Laird, J.R.; Khanna, N.N.; Mavrogeni, S.; et al. The present and future of deep learning in radiology. *Eur. J. Radiol.* **2019**, *114*, 14–24. [[CrossRef](#)] [[PubMed](#)]
25. Fu, Y.; Lei, Y.; Wang, T.; Curran, W.J.; Liu, T.; Yang, X. Deep learning in medical image registration: A review. *Phys. Med. Biol.* **2020**, *65*, 20TR01. [[CrossRef](#)] [[PubMed](#)]
26. McBee, M.P.; Awan, O.A.; Colucci, A.T.; Ghobadi, C.W.; Kadom, N.; Kansagra, A.P.; Tridandapani, S.; Auffermann, W.F. Deep learning in radiology. *Acad. Radiol.* **2018**, *25*, 1472–1480. [[CrossRef](#)] [[PubMed](#)]
27. Połap, D.; Woźniak, M.; Damaševičius, R.; Wei, W. Chest radiographs segmentation by the use of nature-inspired algorithm for lung disease detection. In Proceedings of the 2018 IEEE Symposium Series on Computational Intelligence, SSCI 2018, Bengaluru, India, 18–21 November 2018; pp. 2298–2303.
28. Capizzi, G.; Sciuto, G.L.; Napoli, C.; Polap, D.; Wozniak, M. Small Lung Nodules Detection Based on Fuzzy-Logic and Probabilistic Neural Network with Bioinspired Reinforcement Learning. *IEEE Trans. Fuzzy Syst.* **2020**, *28*, 1178–1189. [[CrossRef](#)]
29. Akram, T.; Attique, M.; Gul, S.; Shahzad, A.; Altaf, M.; Naqvi, S.S.R.; Damaševičius, R.; Maskeliūnas, R. A novel framework for rapid diagnosis of COVID-19 on computed tomography scans. *Pattern Anal. Appl.* **2021**, *4*, 951–964. [[CrossRef](#)]
30. Abiyev, R.H.; Ma'aitah, M.K.S. Deep convolutional neural networks for chest diseases detection. *J. Healthc. Eng.* **2018**, *2018*, 4168538. [[CrossRef](#)]
31. Ye, Z.; Zhang, Y.; Wang, Y.; Huang, Z.; Song, B. Chest CT manifestations of new coronavirus disease 2019 (COVID-19): A pictorial review. *Eur. Radiol.* **2020**, *30*, 4381–4389. [[CrossRef](#)]
32. Lee, S.M.; Seo, J.B.; Yun, J.; Cho, Y.H.; Vogel-Claussen, J.; Schiebler, M.L.; Gefter, W.B.; Van Beek, E.J.; Goo, J.M.; Lee, K.S.; et al. Deep learning applications in chest radiography and computed tomography. *J. Thorac. Imaging* **2019**, *34*, 75–85. [[CrossRef](#)]
33. Hashmi, M.F.; Katiyar, S.; Keskar, A.G.; Bokde, N.D.; Geem, Z.W. Efficient pneumonia detection in chest x-ray images using deep transfer learning. *Diagnostics* **2020**, *10*, 417. [[CrossRef](#)] [[PubMed](#)]
34. Wu, J.; Wu, X.; Zeng, W.; Guo, D.; Fang, Z.; Chen, L.; Huang, H.; Li, C. Chest CT findings in patients with coronavirus disease 2019 and its relationship with clinical features. *Investig. Radiol.* **2020**, *55*, 257. [[CrossRef](#)] [[PubMed](#)]
35. Xie, X.; Zhong, Z.; Zhao, W.; Zheng, C.; Wang, F.; Liu, J. Chest CT for typical coronavirus disease 2019 (COVID-19) pneumonia: Relationship to negative RT-PCR testing. *Radiology* **2020**, *296*, E41–E45. [[CrossRef](#)] [[PubMed](#)]
36. Raptis, C.A.; Hammer, M.M.; Short, R.G.; Shah, A.; Bhalla, S.; Bierhals, A.J.; Filev, P.D.; Hope, M.D.; Jeudy, J.; Kligerman, S.J.; et al. Chest CT and coronavirus disease (COVID-19): A critical review of the literature to date. *Am. J. Roentgenol.* **2020**, *215*, 839–842. [[CrossRef](#)]
37. Saglani, S.; Custovic, A. Childhood asthma: Advances using machine learning and mechanistic studies. *Am. J. Respir. Crit. Care Med.* **2019**, *199*, 414–422. [[CrossRef](#)]
38. Amaral, J.L.; Lopes, A.J.; Veiga, J.; Faria, A.C.; Melo, P.L. High-accuracy detection of airway obstruction in asthma using machine learning algorithms and forced oscillation measurements. *Comput. Methods Prog. Biomed.* **2017**, *144*, 113–125. [[CrossRef](#)]
39. Cavailles, A.; Melloni, B.; Motola, S.; Dayde, F.; Laurent, M.; Le Lay, K.; Caumette, D.; Luciani, L.; Lleu, P.L.; Berthon, G.; et al. Identification of patient profiles with high risk of hospital re-admissions for Acute COPD Exacerbations (AECOPD) in France using a machine learning model. *Int. J. Chronic Obstr. Pulm. Dis.* **2020**, *15*, 949. [[CrossRef](#)]
40. Nikolaou, V.; Massaro, S.; Fakhimi, M.; Stergioulas, L.; Price, D. COPD phenotypes and machine learning cluster analysis: A systematic review and future research agenda. *Respir. Med.* **2020**, *171*, 106093. [[CrossRef](#)]
41. Wu, J.; Zan, X.; Gao, L.; Zhao, J.; Fan, J.; Shi, H.; Wan, Y.; Yu, E.; Li, S.; Xie, X. A machine learning method for identifying lung cancer based on routine blood indices: Qualitative feasibility study. *JMIR Med. Inform.* **2019**, *7*, e13476. [[CrossRef](#)]
42. Chakraborty, T.; Ghosh, I. Real-time forecasts and risk assessment of novel coronavirus (COVID-19) cases: A data-driven analysis. *Chaos Solitons Fractals* **2020**, *135*, 109850. [[CrossRef](#)]
43. Alakus, T.B.; Turkoglu, I. Comparison of deep learning approaches to predict COVID-19 infection. *Chaos Solitons Fractals* **2020**, *140*, 110120. [[CrossRef](#)]

44. Salgotra, R.; Gandomi, M.; Gandomi, A.H. Evolutionary modelling of the COVID-19 pandemic in fifteen most affected countries. *Chaos Solitons Fractals* **2020**, *140*, 110118. [[CrossRef](#)]
45. Lorencin, I.; Baressi Šegota, S.; Andelić, N.; Blagojević, A.; Šušteršić, T.; Protić, A.; Arsenijević, M.; Čabov, T.; Filipović, N.; Car, Z. Automatic Evaluation of the Lung Condition of COVID-19 Patients Using X-ray Images and Convolutional Neural Networks. *J. Pers. Med.* **2021**, *11*, 28. [[CrossRef](#)] [[PubMed](#)]
46. Grillo, F.; Barisione, E.; Ball, L.; Mastracci, L.; Fiocca, R. Lung fibrosis: An undervalued finding in COVID-19 pathological series. *Lancet Infect. Dis.* **2021**, *21*, e72. [[CrossRef](#)]
47. Blagojević, A.; Šušteršić, T.; Lorencin, I.; Šegota, S.B.; Milovanović, D.; Baskić, D.; Baskić, D.; Car, Z.; Filipović, N. Combined machine learning and finite element simulation approach towards personalized model for prognosis of COVID-19 disease development in patients. *EAI Endorsed Trans. Bioeng. Bioinform.* **2021**, *1*, e6.
48. Saba, A.I.; Elsheikh, A.H. Forecasting the prevalence of COVID-19 outbreak in Egypt using nonlinear autoregressive artificial neural networks. *Process Saf. Environ. Prot.* **2020**, *141*, 1–8. [[CrossRef](#)] [[PubMed](#)]
49. Salgotra, R.; Gandomi, M.; Gandomi, A.H. Time series analysis and forecast of the COVID-19 pandemic in India using genetic programming. *Chaos Solitons Fractals* **2020**, *138*, 109945. [[CrossRef](#)]
50. Elmousalam, H.H.; Hassanien, A.E. Day level forecasting for Coronavirus Disease (COVID-19) spread: Analysis, modeling and recommendations. *arXiv* **2020**, arXiv:2003.07778.
51. Car, Z.; Baressi Šegota, S.; Andelić, N.; Lorencin, I.; Mrzljak, V. Modeling the spread of COVID-19 infection using a multilayer perceptron. *Comput. Math. Methods Med.* **2020**, *2020*, 5714714. [[CrossRef](#)]
52. Rizk-Allah, R.M.; Hassanien, A.E. COVID-19 forecasting based on an improved interior search algorithm and multi-layer feed forward neural network. *arXiv* **2020**, arXiv:2004.05960.
53. Hasan, N. A methodological approach for predicting COVID-19 epidemic using EEMD-ANN hybrid model. *Internet Things* **2020**, *11*, 100228. [[CrossRef](#)]
54. Sujath, R.; Chatterjee, J.M.; Hassanien, A.E. A machine learning forecasting model for COVID-19 pandemic in India. *Stoch. Environ. Res. Risk Assess.* **2020**, *34*, 959–972. [[CrossRef](#)] [[PubMed](#)]
55. Vaid, S.; Cakan, C.; Bhandari, M. Using machine learning to estimate unobserved COVID-19 infections in North America. *J. Bone Jt. Surg. Am. Vol.* **2020**, *102*, e70. [[CrossRef](#)] [[PubMed](#)]
56. Melin, P.; Monica, J.C.; Sanchez, D.; Castillo, O. Multiple ensemble neural network models with fuzzy response aggregation for predicting COVID-19 time series: The case of Mexico. *Healthcare* **2020**, *8*, 181. [[CrossRef](#)] [[PubMed](#)]
57. Rayungsari, M.; Aufin, M.; Imamah, N. Parameters estimation of generalized richards model for covid-19 cases in indonesia using genetic algorithm. *Jambura J. Biomath. (JJBM)* **2020**, *1*, 25–30. [[CrossRef](#)]
58. Pontoh, R.S.; Toharudin, T.; Zahroh, S.; Supartini, E. Effectiveness of the public health measures to prevent the spread of covid-19. *Commun. Math. Biol. Neurosci.* **2020**, *2020*, 31.
59. Kuwimy, C.; Nazari, F.; Jiao, X.; Rohani, P.; Nataraj, C. Nonlinear dynamic analysis of an epidemiological model for COVID-19 including public behavior and government action. *Nonlinear Dyn.* **2020**, *101*, 1545–1559. [[CrossRef](#)]
60. Andelić, N.; Baressi Šegota, S.; Lorencin, I.; Mrzljak, V.; Car, Z. Estimation of COVID-19 epidemic curves using genetic programming algorithm. *Health Inform. J.* **2021**, *27*, 1460458220976728. [[CrossRef](#)]
61. Ardabili, S.; Mosavi, A.; Band, S.S.; Varkonyi-Koczy, A.R. Coronavirus disease (COVID-19) global prediction using hybrid artificial intelligence method of ANN trained with Grey Wolf optimizer. In Proceedings of the 2020 IEEE 3rd International Conference and Workshop in Óbuda on Electrical and Power Engineering (CANDO-EPE), Budapest, Hungary, 18–19 November 2020; pp. 000251–000254.
62. González, G.; Ash, S.Y.; Vegas-Sánchez-Ferrero, G.; Onieva, J.O.; Rahaghi, F.N.; Ross, J.C.; Díaz, A.; Estépar, R.S.J.; Washko, G.R. Disease Staging and Prognosis in Smokers Using Deep Learning in Chest Computed Tomography. *Am. J. Respir. Crit. Care Med.* **2018**, *197*, 193–203. [[CrossRef](#)]
63. Basu, S.; Mitra, S.; Saha, N. Deep learning for screening covid-19 using chest x-ray images. In Proceedings of the 2020 IEEE Symposium Series on Computational Intelligence (SSCI), Canberra, ACT, Australia, 1–4 December 2020; pp. 2521–2527.
64. Albahli, S. A Deep Neural Network to Distinguish COVID-19 from other Chest Diseases Using X-ray Images. *Curr. Med. Imaging Former. Curr. Med. Imaging Rev.* **2021**, *17*, 109–119. [[CrossRef](#)]
65. Bernheim, A.; Mei, X.; Huang, M.; Yang, Y.; Fayad, Z.A.; Zhang, N.; Diao, K.; Lin, B.; Zhu, X.; Li, K.; et al. Chest CT Findings in Coronavirus Disease-19 (COVID-19): Relationship to Duration of Infection. *Radiology* **2020**, *295*, 200463. [[CrossRef](#)] [[PubMed](#)]
66. Choudhary, P.; Hazra, A. Chest disease radiography in twofold: Using convolutional neural networks and transfer learning. *Evol. Syst.* **2019**, *12*, 567–579. [[CrossRef](#)]
67. Chandra, T.B.; Verma, K. Pneumonia detection on chest x-ray using machine learning paradigm. In Proceedings of the 3rd International Conference on Computer Vision and Image Processing, Jabalpur, India, 29 Sepember–1 October 2018; Springer: Berlin/Heidelberg, Germany, 2020; pp. 21–33.
68. Anjum, M.A.; Amin, J.; Sharif, M.; Khan, H.U.; Malik, M.S.A.; Kadry, S. Deep semantic segmentation and multi-class skin lesion classification based on convolutional neural network. *IEEE Access* **2020**, *8*, 129668–129678. [[CrossRef](#)]

69. Hussain, E.; Hasan, M.; Rahman, M.A.; Lee, I.; Tamanna, T.; Parvez, M.Z. CoroDet: A deep learning based classification for COVID-19 detection using chest X-ray images. *Chaos Solitons Fractals* **2021**, *142*, 110495. [[CrossRef](#)] [[PubMed](#)]
70. Rahman, T.; Chowdhury, M.E.; Khandakar, A.; Islam, K.R.; Islam, K.F.; Mahbub, Z.B.; Kadir, M.A.; Kashem, S. Transfer learning with deep convolutional neural network (CNN) for pneumonia detection using chest X-ray. *Appl. Sci.* **2020**, *10*, 3233. [[CrossRef](#)]